

Optimization Framework for a Large, High Speed Bearingless Permanent Magnet Motor

Ye gu Kang, Eric L. Severson

Department of Electrical and Computer Engineering
University of Wisconsin-Madison, Madison, WI, USA
E-mail: eric.severson@wisc.edu

Abstract—Recently, there has been increased research interest in developing higher power bearingless motors. To reach significant power levels, rigorous design optimization is needed. This paper investigates the electromagnetic design space for a 30k r/min, 50kW bearingless permanent magnet motor. The differential evolution optimization algorithm is used to optimize two different design topologies for various objective functions. Detailed modeling considerations are presented to calculate the key performance metrics which are unique to bearingless motor designs (i.e., average and ripple suspension forces) in a computationally efficient manner. The resulting optimal design geometry is compared to demonstrate the wide design space of this machine. Finally, a weighted multi-objective function is proposed based on efficiency, force and torque ripple, and power density.

NOMENCLATURE

A_L	Linear current density (kA/m)
B_g	No load air gap field (Tesla)
D_{os}	Outer stator diameter (mm)
D_{or}	Outer rotor diameter (mm)
E_a	Force angle error (degrees)
E_m	Force amplitude error normalized by desired force magnitude
FRW	Force per unit of rotor weight
L_g	Airgap length (mm)
L_{st}	Stack length (mm)
O_m	Objective function variable m
P_a	Penalty function
P_c	Core loss (W)
PR	Pole arc ratio
Q	Number of stator slots
SR	Slot ratio
S_1	Shoe height 1 (mm)
S_2	Shoe height 2 (mm)
T_m	Permanent magnet thickness (mm)
T_r	Torque ripple normalized by average torque
TRV	Torque per unit of rotor volume
T_s	Stator yoke thickness (mm)
W_t	Tooth width (mm)
w_m	Weighting factor for objective function variable m
η	Machine efficiency

I. INTRODUCTION

Active magnetic bearings have been commercialized to provide a non-contact solution for supporting motor shafts.

Compared to contact-type bearings, this has advantages in extreme reliability, lifetime, and efficiency. However, achievable magnetic force densities are low compared to contact-type bearings, yielding bulky machine designs which have been particularly problematic at high speeds. Alternatively, bearingless motors create magnetic bearing forces in the airgap of an electric motor by modifying the motor's magnetic field. This allows for the elimination of one or more magnetic actuators, potentially solving the aforementioned problem [1].

Bearingless motors have so-far been developed for specialized applications, such as artificial hearts, hygienic pumps, and hygienic mixing devices, where the contact free and integrated operation has been of greater importance than achieving significant power and efficiency levels [2]–[4]. Recently, several initiatives have looked at developing bearingless motors for industrial compressor applications where significant power, efficiency, and speed are needed (i.e., > 30 kW, $> 95\%$, and > 20 k r/min), for example: [5]–[8]. Satisfying the contradictory requirements of magnetic suspension and motor performance at this speed range has proven quite challenging. Investigations have so far focused on exploring design topologies and suggesting metrics to assess a bearingless design. The trend has been to explore the design space by fixing all design variables except for a single variable of interest, which is then varied over a range of permissible values to gain insight into how that variable impacts the design metrics and whether the design topology can be made viable. Particularly, in [6], [7], interesting design knowledge has been developed into workable rotor topologies that yield promising torque/force density and ripple performance.

This paper takes the advancements of [6], [7] and re-frames the problem as a multi-objective design optimization problem. In this study, the differential evaluation (DE) optimization technique is used to search the design space by leveraging 2D finite element analysis (FEA) to consider coupling and saturation effects. This investigation explores the suitability of various objective functions to evaluate bearingless permanent magnet synchronous motor (BPM SM) designs based on the following key performance parameters: torque density, force density, torque ripple, force angle and amplitude error, and machine efficiency. The various objective functions are shown to yield substantially different design geometry, with trade-offs in the magnetic suspension and motor performance. Two rotor geometries are considered that are similar to what is described in [7]: a “pure” surface mount topology and an inset topology

where iron teeth are located between the magnets.

The core contribution of this paper is to use the differential evolution optimization algorithm to explore the design space of the BPMSM for industrial compressor applications. Differences between conventional PM motor design are identified as well trends in design variables that are unique to bearingless motors.

II. MOTOR MODEL

Details of the motor topology considered in this investigation are now described, including the motor topology and parameters used to define the geometry.

A. Motor and Winding Topology

The bearingless motor topology optimized in this paper is a surface mount permanent magnet motor with four rotor poles ($p = 2$) and 6 stator slots ($Q = 6$). The stator is wound as a fractional-slot concentrated winding. In addition to producing torque, the winding is configured to produce a suspension field of 2 poles ($p_s = 1$). The design of this bearingless motor topology has also been considered in [7].

The stator winding can be realized as two separate windings (a torque and a suspension winding) or as a single combined winding (where the same coils produce both torque and suspension forces) [9], [10]. In [10], it is shown that this winding can be implemented as a DPNV-type combined winding (parallel combined winding) with the same winding factors as it would have if implemented as a separated winding. The combined winding approach is advantageous from a motor performance perspective because it allows the drive to dynamically allocate slot current between creating suspension forces and creating torque. The drive connection and operation for DPNV windings is described in [11]. Since the combined winding and separated winding approaches produce the same slot current for this bearingless motor, the design modeling does not need to distinguish between the two approaches. Rather, in this paper, the total slot current is set according to the amount of torque and suspension force that must be produced.

B. Model parameters

To enable exploring several different optimization functions in a meaningful and insightful manner, the design space is highly constrained with relatively few independent variables (8 variables are optimized, as opposed to the 17 variables identified in [12]) which are now described. This investigation considers two rotor structures for the BPMSM: a standard SPMSM rotor (rotor type 1) and an inset magnet rotor (rotor type 2). The radial cross-section of the motor for either rotor structure is described by the same 10 independent variables. Fig. 1 and Fig. 2 depict the definition of these variables for each rotor structure. This paper treats θ_t and θ_s as a single independent variable defined in (1), where $\theta_s = 60^\circ$ (due to

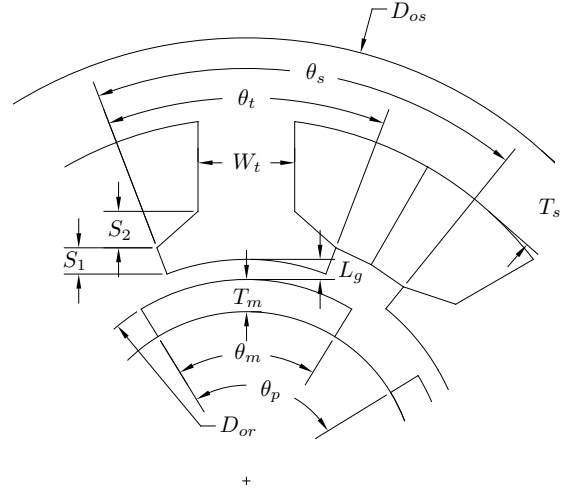


Fig. 1. BPMSM geometry with rotor type 1 (type R1).

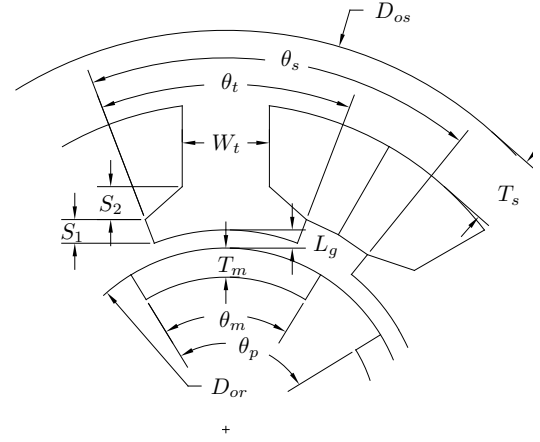


Fig. 2. BPMSM geometry with rotor type 2 (type R2).

the design having 6 slots). Similarly, θ_m and θ_p are a single variable defined in (2).

$$SR = \frac{\theta_t}{\theta_s} \quad (1)$$

$$PR = \frac{\theta_m}{\theta_p} \quad (2)$$

Of these 10 variables, 8 are determined by the optimization algorithm (listed in Table I along with their allowable range), while the remaining two variables (D_{or} and D_{os}) are held constant as described below. Note that the parameters SR , PR , S_1 , and S_2 are defined to allow the optimization algorithm to tune the airgap field harmonic content, which has a significant impact on the suspension force performance.

A maximum rotor tip speed of 150 m/s is assumed at the surface of the permanent magnets and a 3mm thick nonconductive sleeve is used to retain the permanent magnets on the rotor. This tip speed and sleeve thickness are typical values that can be expected for a high performance SPMSM motor design [7], [13]–[15]. For the rated rotational speed

TABLE I. GEOMETRIC CONSTRAINTS

Symbol	Min. value	Max. value	Initial value
L_g	3.3	9	6
T_m	1.5	8	4
W_t	20	40	35
T_s	15	35	20
S_1	3	10	5
S_2	3	10	5
SR	0.5	0.9	0.7
PR	0.5	0.9	0.7

TABLE II. DESIGN INFORMATION

Permanent magnet	N40H
Laminations	Arnon5
Lamination Stacking Factor	0.91
Magnet wire	Copper
Sleeve	3mm Carbon fiber
Conductor Current Density	$3.7A_{rms}/mm^2$
Slot packing factor	0.45
Rated Power	50 kW
Rated Speed	30,000 r/min

of 30,000 r/min, this corresponds to a rotor diameter of $D_{or} = 95.5mm$. In addition to this, the stator outer diameter is fixed at $D_{os} = 250mm$ to restrict the design space size, and facilitate intuitive comparisons between designs.

Additional model parameters and design ratings are summarized in Table II.

III. DESIGN PERFORMANCE CALCULATIONS

Techniques and assumptions used to model and calculate the performance metrics of the BPMSM are now described. Emphasis is placed on considerations that are unique to a bearingless motor design (i.e., effects related to the magnetic suspension field). A 2D static finite element analysis (FEA) package (FEMM [16]) calculates the machine's magnetic field, which is then used to make loss and force calculations. Simplifying assumptions are employed whenever reasonable to enable computationally efficient performance calculations.

A. Losses

Iron, copper, and air friction loss calculations are needed to evaluate the efficiency of each BPMSM design. Note that this list of loss components differs from that of a conventional motor design in that no bearing losses are present in bearingless motors.

Since a population based optimization method is used (differential evolution), thousands of designs will be evaluated throughout the optimization process. To achieve a reasonable design time, computationally efficient loss calculations are necessary. This section describes the loss calculation assumptions and methodology.

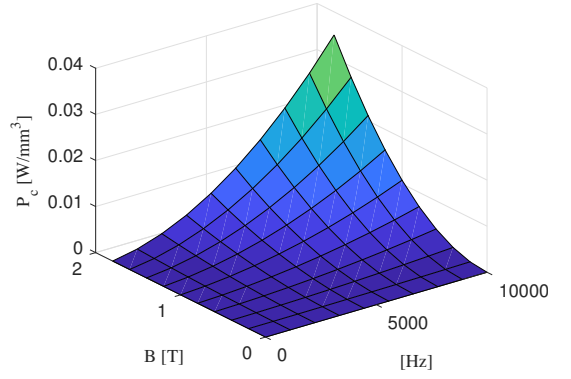


Fig. 3. Lamination core losses as a function of excitation and frequency.

1) *Copper Loss*: Coil loss is calculated as the ohmic loss caused by the slot current density over the slot area. This is calculated from (3), where N is the number of turns within a slot, L_c is an estimate of the total coil length, I is the coil current, and A_c is the cross-sectional area of a conductor. The calculations assume AC effects to be negligible (i.e., thin, transposed conductors).

$$P_{cu} = \rho_{cu} \frac{L_c}{A_c} I^2 N Q \quad (3)$$

2) *Permanent Magnet Loss*: Magnet eddy current losses are calculated following the procedure outlined in [17] and using a Matlab function provided with FEMM [16].

3) *Iron Loss*: To calculate iron losses (stator and rotor laminations), loss data for the lamination material has been extracted from the manufacture's datasheet [18] and curve fit to the well-known Steinmetz Equation (4), shown in Fig. 3.

$$P_c = C_h \omega_e B^2 + C_e \omega_e^2 B^2 \quad (4)$$

The following iron loss calculation procedure is followed:

- 1) field data for each mesh element located in the lamination material is extracted from the FEA solver;
- 2) the harmonic components for the field in each element are calculated;
- 3) the core loss per unit length of each harmonic component in each element is calculated from (4);
- 4) the total core loss per unit length is calculated by summing all of the core loss values (from step 3);
- 5) the result is multiplied by the stack length of the motor to obtain the final core loss.

4) *Air friction Loss*: The approach to calculating air friction loss relies on pre-calculated air friction coefficients. These coefficients can be obtained from experimental measurement and are selected based on the well-known Reynolds and Taylor numbers depending on the flow condition [19]–[22].

The air friction losses on the rotor's radial surface are calculated using the approach presented in [20] with the same

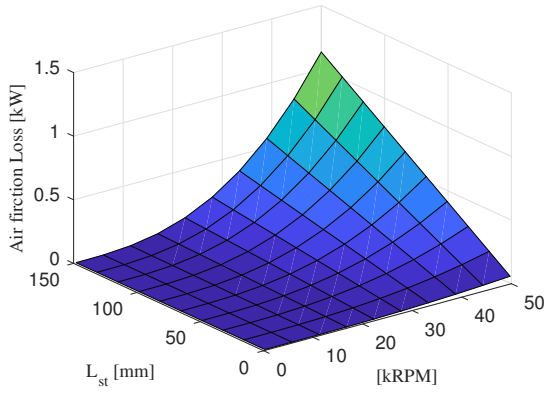


Fig. 4. Air friction losses for a design with a fixed airgap length while speed and stack length are varied.

loss coefficients, using (5). In this expression, C_{fr} is the radial surface air loss coefficient, ρ_a is the temperature-dependent density of air, and ω is the angular velocity of the rotor. The air friction losses on the axial surface of the rotor are calculated using the approach presented in [22] and are calculated as (6), where C_{fa} is the axial surface air loss coefficient. For designs with a large aspect ratio (large values of D_{os}/L_{st}), these end surface losses become increasingly important.

$$P_{wr} = \pi C_{fr} \rho_a \omega^3 \left(\frac{D_{or}}{2} + 0.003 \right)^4 L_{st} \quad (5)$$

$$P_{wa} = \frac{1}{2} C_{fa} \rho_a \omega^3 \left(\frac{D_{or}}{2} + 0.003 \right)^5 \quad (6)$$

With this investigation's assumption of fixed rotor diameter D_{or} , the key input variables to calculate windage losses are the airgap length L_g and stack length L_s . Depending on the objective function used for the design optimization, different torque or force density values may be found, which will require the stack length to scale in order to achieve the rated design power. Longer stack lengths correspond to higher air friction loss. Further, the temperature of the air is assumed to vary linearly with the rotational speed from 20°C to 120°C. Example windage loss calculations for a bearingless motor design with a fixed airgap are shown as a function of stack length and rotational speed in Fig. 4.

B. Force and torque calculations

Torque and force ripple values are important considerations when evaluating a BPMSM design. Torque ripple T_r contributes to the same undesirable performance that has been thoroughly studied in traditional motor design – namely, vibration and acoustic noise.

Force ripple is a unique consideration to bearingless motor design. It can be viewed in terms of an amplitude error and angle error [23]. That is, the instantaneous force vector that is produced may differ from the desired force vector in terms of both its amplitude and angle. The error amplitude and angle

will fluctuate over the course of one rotor revolution due to space harmonics in the magnetizing field (slotting effect and saturation) and due to harmonics in the winding MMF. Fig. 8 depicts these force error quantities for a desired force vector in the x -direction at an instant of time. Large maximum error angles can result in oscillations and instability in the levitation control. It is suggested in [1], [6], [7], [24], that designs attempt to minimize the maximum error angle that is observed over one revolution to be within 5°.

Since both torque and force ripple vary with rotor rotation, multiple static solves are required at different rotor angles in order to quantify the maximum ripple values. To investigate the minimum number of rotor angles required, example bearingless motor designs are solved at rotor angle increments of 1 degree and harmonic components are calculated for the force and torque waveforms. To allow for the possibility that different BPMSM designs have different harmonic content, 70 designs of rotor type 1 were evaluated where the independent design parameters were randomly selected within the ranges listed in Table IV. Fig. 5 shows the harmonic components of the torque waveform. Clearly, the lowest order harmonic of significant interest is the 6th harmonic. This is a well-known property of electric machines [25] and means that any 60° span of rotor angles can be used to determine the entire torque waveform. Within that 60° span, torque is calculated at 6 evenly spaced rotor angles (a sampling resolution of 10° is used), which is a common practice in motor design. The peak-to-peak torque value is then calculated as the difference between the maximum and minimum of these torque data points and normalized by the average torque.

A similar process is repeated for analyzing the required sampling frequency of the force waveform. Fig. 6 shows the force harmonic components of the 70 random BPMSM designs when suspension currents are injected at the synchronous frequency (to create a constant magnitude and direction force). The lowest harmonic component observed is the 2nd harmonic, which means that a 180° span of rotor angles must be evaluated. To determine the required sample resolution, the maximum error angle calculated for different values is studied. Accurate calculations of the error angle are particularly important because inaccuracies larger than 1° have significant implications for whether a design is acceptable (whether it meets the criteria that $E_a \leq 5^\circ$).

The procedure to calculate the error angle is as follows (Referring to Fig. 8):

- 1) the model is solved for the 180° span of rotor angles with rated torque and suspension current;
- 2) at each point, the angle of the suspension force vector is calculated;
- 3) for each design, the desired suspension force vector \vec{F}_c is calculated as the average of the vectors from step 2 (this decouples the effect of torque armature current on the suspension forces);
- 4) the error angle is determined for each sample point by

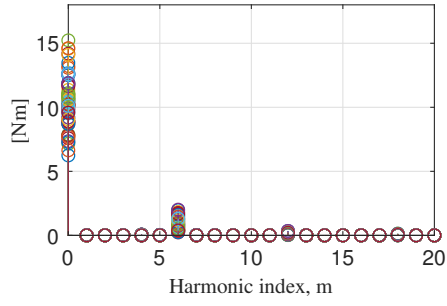


Fig. 5. FFT result of torque waveform calculated for one rotor revolution

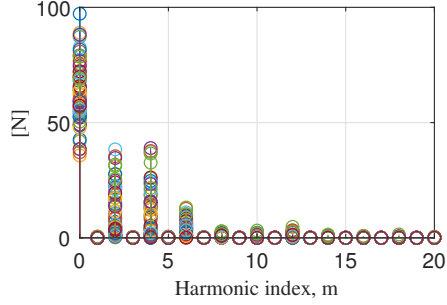


Fig. 6. FFT result of force waveform calculated for one rotor revolution

subtracting the sample point's force vector angle from the angle of \vec{F}_c ;

- 5) the maximum angle magnitude found in step 4 is the maximum error angle E_a .

Maximum error angle values of the 70 random BPMSM designs are calculated and compared against a design that is sampled at 1° increments. The difference is treated as the uncertainty of the error angle calculation for a given sampling interval and is plotted in Fig. 7. A sampling interval of 10° is selected as having the maximum allowable uncertainty in the error angle, and is used for force calculations. Note that if only 6 equally spaced rotor angles (sample angle of 30° in Fig. 7) were used for error angle calculations (as is done for torque calculations), the maximum uncertainty in the error angle would be unacceptable large ($\approx 7.5^\circ$).

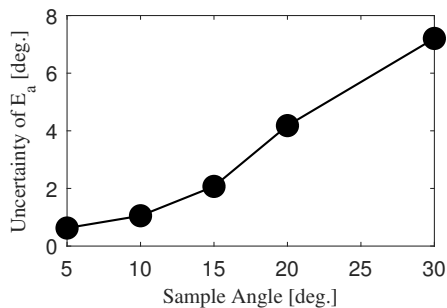


Fig. 7. Uncertainty in the error angle value for different sample intervals

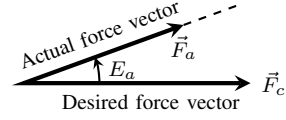


Fig. 8. Desired and actual suspension force vectors.

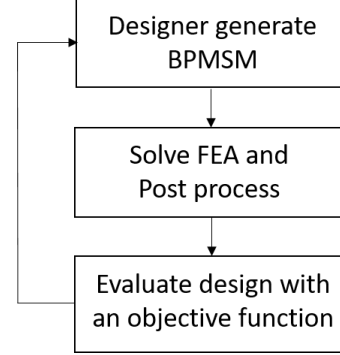


Fig. 9. Design flowchart of BPMSM for an engineer.

IV. OPTIMIZATION

The typical FEA based machine design process flowchart is shown in Fig. 9. The number of iterations can be reduced using machine analytic equations or designer's experience. However, this is a challenging process as the performance variables are typically in a trade-off relationship and the sensitivity of each each performance variable to the design parameters is difficult to anticipate. The flowchart in Fig. 10 shows multi-objective FEA based optimization used in this paper. The iterative process, including model generation and evaluation, is fully automated. Multiple instances of FEA design evaluation are called using the parallel computing toolbox in Matlab to expedite the optimization process.

A. Differential evolution optimization algorithm

Differential evolution (DE), particle swarm (PSO), and genetic algorithms (GA) are commonly used to optimize large, non-convex design spaces, such as that found in electric machine design. This paper uses the DE algorithm. A detailed description of the algorithm is provided in [26], an example of its use in optimizing a PMSM is presented in [27], and an example of its use for optimizing an active magnetic bearing design is presented in [28].

This paper uses the DE algorithm to optimize the BPMSM designs described in Section II. In the algorithm, a cross-over ratio of 0.3 is selected to take into account the parameter dependency and a weighting factor of $F = 0.3$ is used for mutation (7), where \mathbf{v} is an evolved design, and \mathbf{r}_1 , \mathbf{r}_2 , and \mathbf{r}_3 are previously evaluated designs.

$$\mathbf{v} = \mathbf{r}_1 + F(\mathbf{r}_2 - \mathbf{r}_3) \quad (7)$$

B. Multi-Objective Function

To design a high performance bearingless motor, various aspects of the design must be taken into account. The standard

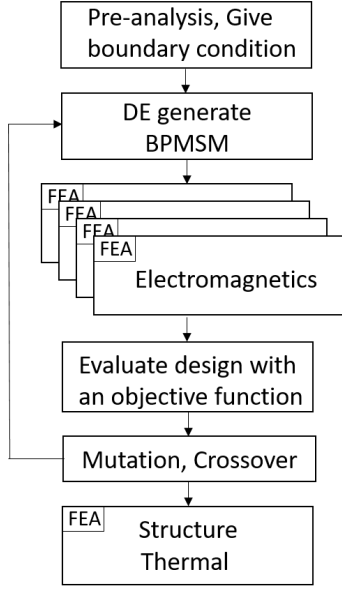


Fig. 10. Multi-physics FEA based DE opt with boundary and pre-defined assumptions.

multi-objective function (8) is utilized to accomplish this.

$$MO = P_a + \sum_{m=1}^6 O_m w_m \quad (8)$$

The same objective function is used for both BPMSM rotor types (type 1 and 2 defined in Section II-B) to facilitate a comparative analysis. Table III defines each of the objective functions used in the optimization, in terms of performance variables and weighting factors. The components of this function are now described in more detail.

1) *Performance variables*: The design performance variables are now described for evaluation of a BPMSM design. In addition to the standard torque metrics, the BPMSM design includes performance variables based on suspension force capabilities. Torque and force density are captured in the TRV and FRW performance variables (defined in the nomenclature table and calculated for rated slot-current). These parameters can be benchmarked against other known designs. For example, TRV of typical high-performance servomotors is 15-50 kNm/m^3 [29]. An FRW value of 1 indicates that rated slot current conditions are able to support the rotor weight. Torque and force ripple performance are captured by the variables T_r , E_a , and E_m with the calculation procedures described in Section III-B, as shown in Table III. The final performance variable is the motor efficiency, which is calculated from the electric, magnetic, and windage losses as described in Section III-A.

2) *Scaling factor*: Scaling factors appear as constant values in the objective definitions of Table III. These constants are used to normalize the objective based on what a “reasonable” design optimization is expected achieve. For example, in O_1 the value $1/TRV$ is scaled by 30 kNm/m^3 so that $O_1 = 1$

for a design with this TRV value. This normalization is done so that the weighting factors can be interpreted as setting the relative importance of each objective.

3) *Weighting factor*: The weighting factor is multiplied with objective variables and summed to evaluate the multi-objective function as shown in (8). Each weighting factor is chosen as the importance of the objective.

4) *Penalty*: A design that does not satisfy the geometric constraints described in Table I is discarded by adding a large penalty P_a to (8).

C. Machine Excitation

Magnet materials and the coil current density are provided in Table II. In the optimization process, each machine is evaluated under rated current conditions, where 97.5% of the slot current density is allocated to torque producing current and 2.5% to suspension force producing current.

D. Evaluation Procedure

Referring to the discussion in Section III, FEMM is used to evaluate the fields of the machine under rated current conditions in 10 degree increments of rotor rotation, over a span of 180° . The field data is used to calculate force, torque, and efficiency performance variables as per length quantities. The length of the machine is then determined so that the machine produces the rated torque (calculated from the rated power and speed provided in Table II) and the final performance variables are calculated using this length.

V. OPTIMIZATION RESULTS

The design space of the BPMSM is investigated with four sets of objective functions (see Table III) and two rotor types (see Fig. 1 and Fig. 2). Results of the first two optimization functions (T and TF1 in Table III) highlight the difference between conventional PM motor design and BPMSM design. Results from the next two optimization functions (TF2 and TFE) are used to explore trends in design variables that are unique to bearingless motors. The only differences between each of the optimization runs are in the weighting factors (as defined in Table III). These changes are found to yield to very different designs, which can be clearly seen Fig. 11. The optimized geometric parameters for each objective function are shown in Table IV and the corresponding performance variables are shown in Table V. Detailed analysis of the results of each optimization run are now presented.

A. Torque optimization

1) *T*: The first optimization function optimizes only the torque generation capability, without regard to the suspension force requirements. In this case, the optimization framework places emphasis on tuning the stator tooth dimensions to maximize the torque producing airgap flux density and minimize harmonics that lead to torque ripple. In comparing rotor designs R1 and R2, it can immediately be seen that R2

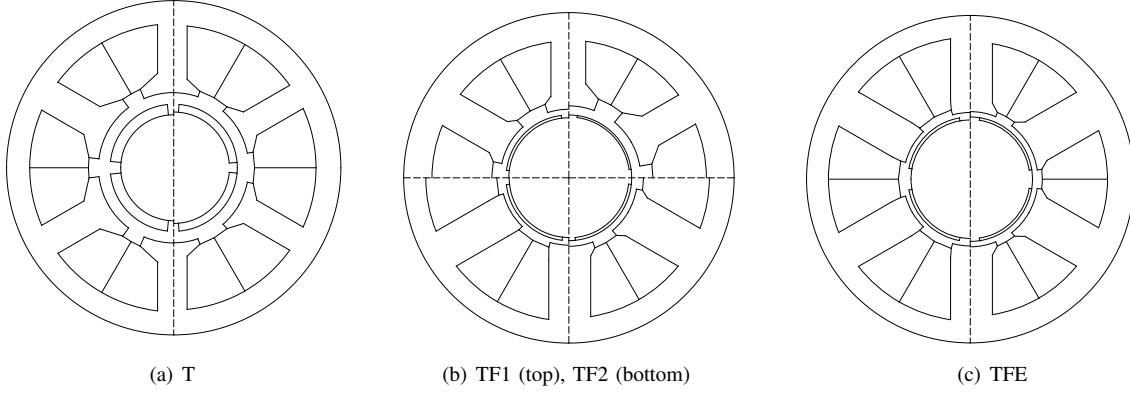


Fig. 11. BPMSM cross-section results for each of the optimization functions defined in Table III. The left side of each figure corresponds to rotor type R1 and the right side to rotor type R2.

TABLE III. OBJECTIVE FUNCTION DEFINITIONS

Objectives		Optimization functions explored				
		Weight	T ^a	TF1 ^b	TF2 ^c	TFE ^d
O_1	$30e3/TRV$	w_1	1	1	1	1
O_2	$1/FRW$	w_2	0	1	1	1
O_3	$T_r/0.05$	w_3	1	1	0.1	0.1
O_4	E_a	w_4	0	1	0.1	0.1
O_5	$E_m/0.05$	w_5	0	1	0.1	0.1
O_6	$1/\eta^2$	w_6	0	0	0	10

^aT: Torque optimization

^bTF1: Torque-force optimization

^cTF2: Torque-force optimization case 2

^dTFE: Torque-force-efficiency optimization

TABLE IV. OPTIMAL GEOMETRIC PARAMETERS FOR EACH OBJECTIVE FUNCTION

	T ^a		TF1		TF2		TFE	
	R1 ^b	R2 ^c	R1	R2	R1	R2	R1	R2
L_g	8.75	8.59	4.35	6.88	3.42	4.30	3.47	4.11
T_m	7.87	5.84	2.08	1.53	2.37	2.12	2.29	1.98
W_t	24.1	20.0	27.2	25.4	30.4	33.0	30.0	33.8
T_s	17.3	18.6	21.5	21.0	16.8	18.7	16.8	20.2
S_1	7.87	6.35	4.69	8.63	9.21	4.75	7.21	5.34
S_2	7.53	4.37	6.56	9.24	3.65	4.69	3.87	3.47
SR	0.77	0.63	0.60	0.69	0.54	0.68	0.51	0.74
PR	0.87	0.89	0.85	0.83	0.86	0.87	0.78	0.80
L_{st}	37.0	41.9	66.5	112.8	48.1	60.4	54.2	66.92

^aOptimization functions defined in Table III

^bR1: Rotor type 1

^cR2: Rotor type 2

converges to thinner magnets T_m . This appears to be needed to reduce the torque ripple caused by the iron rotor teeth increasing the THD of the airgap field. The ratio of O_1w_1 and O_3w_3 also imply the torque ripple components are easier term to be minimized than TRV . Torque ripple is a function of the harmonics of the airgap flux density which can be manipulated via several variables (SR , PR , S_1 , S_2 , T , L_g), whereas in this highly constrained design framework, TRV depends almost exclusively on the fundamental component of airgap flux density, controlled by only T_m and L_g .

TABLE V. OPTIMIZED PERFORMANCE METRICS

	T ^a		TF1		TF2		TFE	
	R1	R2	R1	R2	R1	R2	R1	R2
O_1w_1	0.45	0.51	0.79	1.37	0.59	0.74	0.63	0.78
O_2w_2	0	0	1.29	2.02	0.94	0.96	0.96	0.87
O_3w_3	0.11	0.10	1.32	0.75	0.15	0.17	0.27	0.21
O_4w_4	0	0	0.96	2.12	0.15	0.46	0.01	0.45
O_5w_5	0	0	0.42	0.80	0.07	0.20	0.03	0.18
O_6w_6	0	0	0	0	0	0	10.9	11.2
TRV	67	59	38	22	51	41	47	38
FRW	0.2	0.3	0.8	0.5	1.1	1.0	1.0	1.1
T_r ^b	0.5	0.5	6.6	3.7	7.4	8.5	13	10
E_a ^c	21	21	1.0	2.1	1.5	4.6	1.1	9.1
E_m ^b	39	44	2.1	4.0	3.5	10.0	1.7	4.5
η ^b	—	—	—	—	—	—	95.6	94.6
C ^d	0.6	0.6	4.8	7.1	1.9	2.5	12.9	13.7
B_g	0.6	0.5	0.5	0.4	0.6	0.6	0.6	0.6
A_L	93	101	93	84	108	93	109	89

^aOptimization functions defined in Table III

^bin %

^cin degrees

^dFinal cost

B. Torque Force Optimization

1) *TF1*: Next, torque and force optimization is done for BPMSM design investigation. By having evenly distributed weights of $w_m = 1$, parameter sensitivity and trade-offs can be investigated and compared to the torque optimization case. Pareto plots are drawn to find the relationship between performance variables, with trade-offs identified and analyzed using the pareto fronts in Fig. 12. In Fig. 12(a), a linear relationship between the force angle error and amplitude error can be identified—which means that design changes to improve E_a are likely to also improve E_m . In Fig. 12(b)-12(d) independent relationships between performance variables are observed, which shows that T_r and force error terms, torque density and ripple terms, and force density and force error terms can all be independently optimized. Further, note the distribution of designs in Fig. 12(d). This distribution indicates either that FRW is more sensitive compared to E_a or that E_a

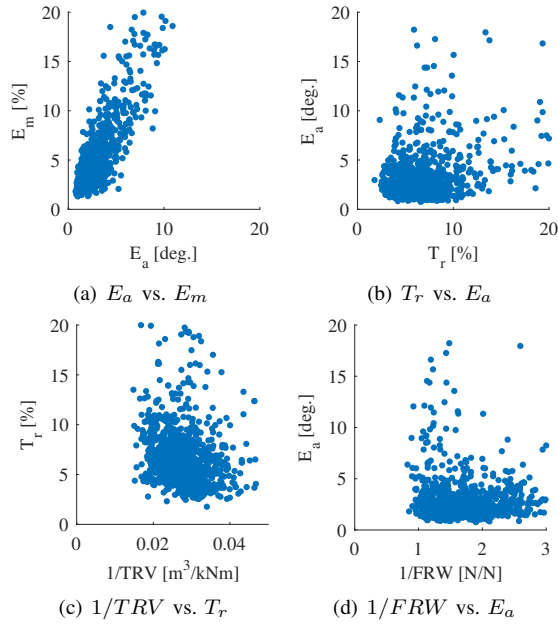


Fig. 12. Pareto plots of performance parameters for TF1 optimization function with rotor type R1.

is relatively easier optimized than FRW (a similar conclusion was drawn for torque and torque ripple in Section V-A).

Input geometric parameter sensitivity on force generation is also investigated shown in Fig. 13. In Fig. 13(a), larger FRW values (better designs) are shown to be obtained for shorter equivalent airgap length values (reduced L_g and T_m), which makes intuitive sense as this reduces the reluctance seen by the armature winding. Interestingly, to minimize force angle error, open slots with low SR values appear to be preferred in Fig. 13(b) (which is the opposite trend observed for minimizing force ripple).

2) *TF2*: Next, the TF2 weighting factors are chosen to achieve a more compact design (higher torque and force density). The resulting BPMSM geometry is shown in Fig. 11(b) and in Table V and Table IV. This optimization results in shorter airgap lengths and thicker magnets, which increases the air gap field (and therefore TRW). Notice that the stator design converged to open slots with low SR values to avoid increasing force error caused by regional saturation of the tooth tip.

The results of TF2 and TF1 are compared in Fig. 14, where several interesting trends can be observed between the two optimization functions as well as between the two rotor structures. The TF2 optimization function clearly worsens ripple components but achieves the best TRV and FRW values. For both algorithms, rotor type R1 performs better in terms of suspension force performance (ripple and force density) and torque density. Further, when comparing the cost (bottom of Fig. 14), rotor type R2 is seen to be generally inferior to type R1. It is therefore concluded that rotor type R1 is superior to rotor type R2 for BPMSM designs.

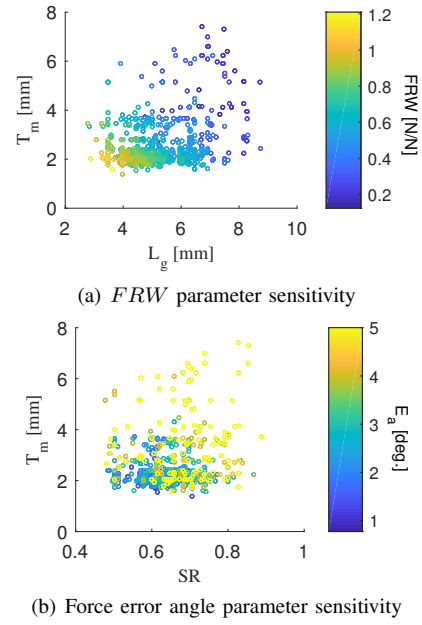


Fig. 13. TF1 optimization rotor type 1 input parameter sensitivity on force generation.

C. Efficiency optimization

1) *TFE*: The fourth objective function uses loss calculations and heavily weights the designs' efficiency. The optimized BPMSM geometry is shown in Fig. 11(c) and again is summarized in Tables V and IV. The emphasis on loss reduction clearly causes the optimization algorithm to reduce the magnet thickness T_m and span PR . Fig. 15(a) shows the loss breakdown of the resulting BPMSM design (rotor type R1) with respect to rotational speed. Notice that the magnet loss is high. Consider the PM has a much smaller volume than the stator, the PM loss has the highest loss density. This is anticipated to cause thermal problems for magnets and will need to be addressed via forced cooling design or mitigated through a more advanced design process that considers the rotor temperature. Addressing magnet thermal challenges is a problem that is common to all high speed SPMSM designs. The efficiency at 30,000 r/min of rotor type 1 is about 96%.

Next, from Fig. 15(b), it can be seen that TRV and efficiency are in a trade-off relationship. The biggest loss components are stator iron loss and magnet loss. When this material is pushed to the limits high TRV is achieved with higher loss. Lower TRV will result in high V_R but lower loss. Note that FRW is independent of TRV and efficiency. Effective airgap length has the most relationship with FRW as shown in Fig. 13(a)

Note when reviewing the performance variables for every iteration, it was observed that for certain designs, the efficiency is greater than 96% and TRV values of up to 60 are observed. However, the best design was selected via the multi-objective function which balanced all competing performance variables.

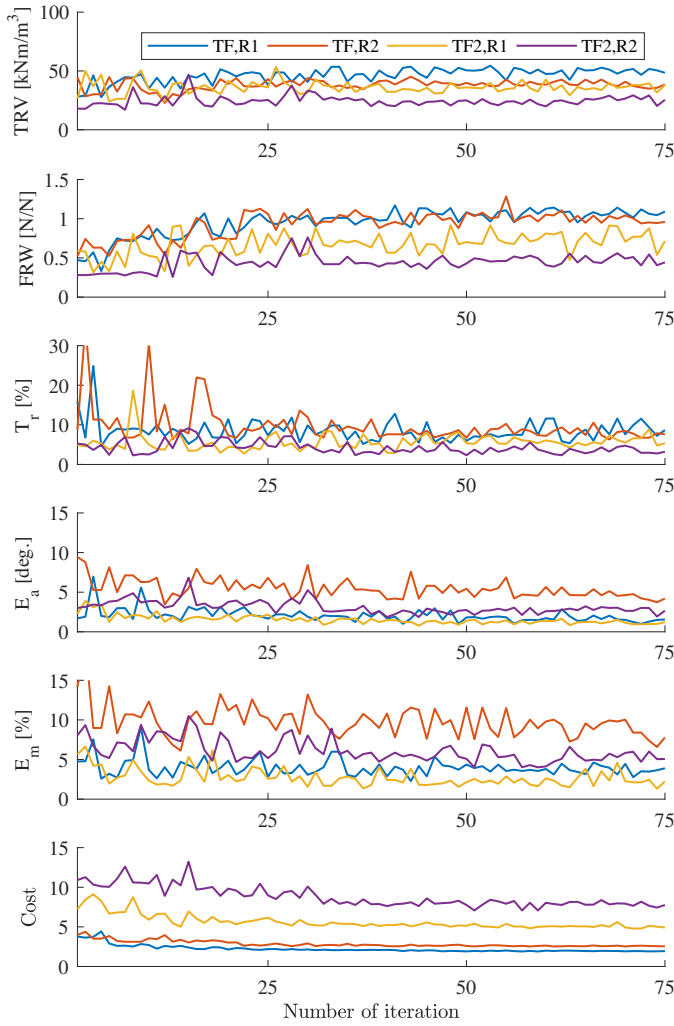


Fig. 14. TF1 and TF2 BPMSM performance parameter values over the 75 iterations that the algorithm is run.

VI. CONCLUSION

This paper has developed and presented a multi-objective optimization framework for a bearingless permanent magnet motor design. The framework is based around the differential evolution algorithm and is shown to be able to automate the entire design process. Design performance variables have been proposed, with emphasis placed on defining and investigating metrics unique to bearingless motors. Whenever possible, computationally efficient design evaluation processes have been developed in order to expedite the optimization process.

The optimal design space of the bearingless motor is explored for two rotor structures with surface mounted magnets. This investigation has been conducted by defining several multi-objective optimization functions that allow design trends to be identified and analyzed. Finally, a balanced multi-objective optimization function is used to demonstrate that a design efficiency of nearly 96% is possible while still satisfying stringent torque and suspension force performance requirements. Future work must focus on considering mechan-

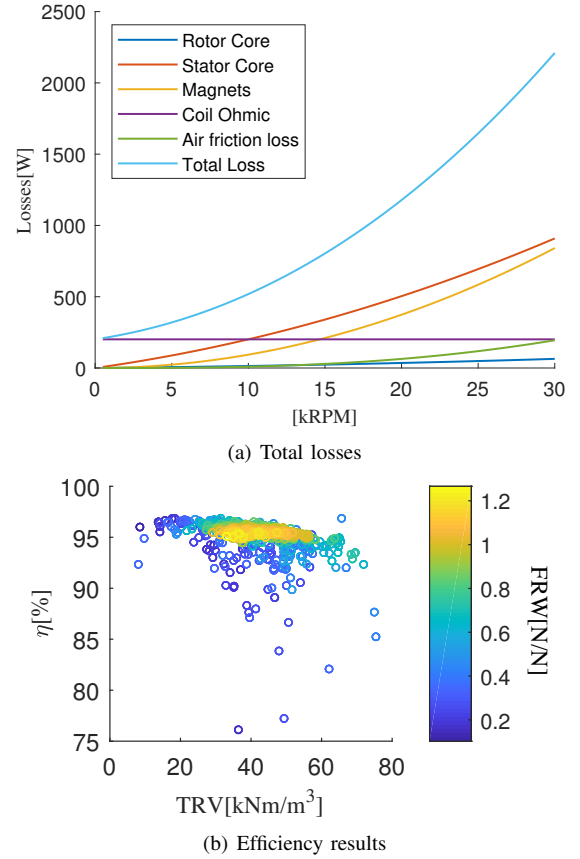


Fig. 15. Results for final TFE optimized design.

ical (structural and thermal) aspects of the design in order to develop a practical motor design.

REFERENCES

- [1] A. Chiba, T. Fukao, O. Ichikawa, M. Oshima, M. Takemoto, and D. Dorrell, *Magnetic Bearings and Bearingless Drives*. Newnes, 2005.
- [2] Y. Okada, N. Yamashiro, K. Ohmori, T. Masuzawa, T. Yamane, Y. Konishi, and S. Ueno, "Mixed flow artificial heart pump with axial self-bearing motor," *Mechatronics, IEEE/ASME Transactions on*, vol. 10, no. 6, pp. 658–665, Dec 2005.
- [3] M. T. Bartholet, T. Nussbaumer, S. Silber, and J. W. Kolar, "Comparative evaluation of polyphase bearingless slice motors for fluid-handling applications," *IEEE Transactions on Industry Applications*, vol. 45, no. 5, pp. 1821–1830, 2009.
- [4] T. Reichert, T. Nussbaumer, and J. Kolar, "Bearingless 300-w pmsm for bioreactor mixing," *Industrial Electronics, IEEE Transactions on*, vol. 59, no. 3, pp. 1376–1388, March 2012.
- [5] R. P. Jastrzebski, P. Jaatinen, A. Chiba, and O. Pyrhnen, "Efficiency of buried permanent magnet type 5kw and 50kw high-speed bearingless motors with 4-pole motor windings and 2-pole suspension windings," in *The 15th International Symposium on Magnetic Bearings (ISMB15)*, Aug 2016, pp. 1–8.
- [6] R. P. Jastrzebski, P. Jaatinen, H. Sugimoto, O. Pyrhnen, and A. Chiba, "Design of a bearingless 100 kw electric motor for high-speed applications," in *Electrical Machines and Systems (ICEMS), 2015 18th International Conference on*, Oct 2015, pp. 2008–2014.
- [7] R. P. Jastrzebski, P. Jaatinen, O. Pyrhnen, and A. Chiba, "Design of 6-slot inset pm bearingless motor for high-speed and higher than 100kw

- applications,” in *Electric Machines and Drives Conference (IEMDC), 2017 IEEE International*. IEEE, 2017, pp. 1–6.
- [8] E. Severson and N. Mohan, “Bearingless motor system design for industrial applications,” in *Electric Machines and Drives Conference (IEMDC), 2017 IEEE International*. IEEE, 2017, pp. 1–8.
- [9] R. P. Jastrzebski, P. Jaatinen, O. Pyrhönen, and A. Chiba, “Current injection solutions for active suspension in bearingless motors,” in *Power Electronics and Applications (EPE’17 ECCE Europe), 2017 19th European Conference on*. IEEE, 2017, pp. P–1.
- [10] E. L. Severson, R. Nilssen, T. Undeland, and N. Mohan, “Design of dual purpose no-voltage combined windings for bearingless motors,” *IEEE Transactions on Industry Applications*, vol. 53, no. 5, pp. 4368–4379, Sept 2017.
- [11] E. Severson, S. Gandikota, and N. Mohan, “Practical implementation of dual-purpose no-voltage drives for bearingless motors,” *IEEE Trans. on Industry Applications*, vol. 52, no. 2, pp. 1509–1518, March 2016.
- [12] B. N. Cassimere and S. D. Sudhoff, “Population-based design of surface-mounted permanent-magnet synchronous machines,” *IEEE Transactions on Energy Conversion*, vol. 24, no. 2, pp. 338–346, 2009.
- [13] A. Binder, T. Schneider, and M. Klohr, “Fixation of buried and surface-mounted magnets in high-speed permanent-magnet synchronous machines,” *IEEE Transactions on Industry Applications*, vol. 42, no. 4, pp. 1031–1037, 2006.
- [14] D. Gerada, A. Mebarki, N. L. Brown, C. Gerada, A. Cavagnino, and A. Boglietti, “High-speed electrical machines: Technologies, trends, and developments,” *IEEE Transactions on Industrial Electronics*, vol. 61, no. 6, pp. 2946–2959, 2014.
- [15] M. van der Geest, H. Polinder, J. A. Ferreira, and M. Christmann, “Power density limits and design trends of high-speed permanent magnet synchronous machines,” *IEEE Transactions on Transportation Electrification*, vol. 1, no. 3, pp. 266–276, 2015.
- [16] D. Meeker, “Finite element method magnetics,” *FEMM*, vol. 4, p. 32, 2010.
- [17] D. Ishak, Z. Zhu, and D. Howe, “Eddy-current loss in the rotor magnets of permanent-magnet brushless machines having a fractional number of slots per pole,” *IEEE Transactions on magnetics*, vol. 41, no. 9, pp. 2462–2469, 2005.
- [18] *Arnold 5 Non Grain Oriented Electrical Silicon Steel Core Loss Chart*, Arnold Magnetica, 2017.
- [19] J. Pyrhonen, T. Jokinen, and V. Hrabovcová, *Design of rotating electrical machines*. Wiley, com, 2009.
- [20] J. An, A. Binder, and C. R. Sabirin, “Loss measurement of a 30 kw high speed permanent magnet synchronous machine with active magnetic bearings,” in *Electrical Machines and Systems (ICEMS), 2013 International Conference on*. IEEE, 2013, pp. 905–910.
- [21] G. Munteanu, A. Binder, and T. Schneider, “Loss measurement of a 40 kw high-speed bearingless pm synchronous motor,” in *Energy Conversion Congress and Exposition (ECCE), 2011 IEEE*. IEEE, 2011, pp. 722–729.
- [22] B. Riemer, M. Leßmann, and K. Hameyer, “Rotor design of a high-speed permanent magnet synchronous machine rating 100,000 rpm at 10kw,” in *Energy Conversion Congress and Exposition (ECCE), 2010 IEEE*. IEEE, 2010, pp. 3978–3985.
- [23] J. Asama, R. Natsume, H. Fukuhara, T. Oiwa, and A. Chiba, “Optimal suspension winding configuration in a homo-polar bearingless motor,” *Magnetica, IEEE Transactions on*, vol. 48, no. 11, pp. 2973–2976, nov. 2012.
- [24] P. Jaatinen, R. P. Jastrzebski, O. Pyrhönen, and A. Chiba, “Improving of bearingless 6-slot ipm motor radial force characteristics using rotor skew,” in *Electric Machines and Drives Conference (IEMDC), 2017 IEEE International*. IEEE, 2017, pp. 1–7.
- [25] D. C. Hanselman, *Brushless permanent magnet motor design*. The Writers’ Collective, 2003.
- [26] K. Price, R. M. Storn, and J. A. Lampinen, *Differential evolution: a practical approach to global optimization*. Springer Science & Business Media, 2006.
- [27] G. Y. Sizov, P. Zhang, D. M. Ionel, N. A. Demerdash, and M. Rosu, “Automated multi-objective design optimization of pm ac machines using computationally efficient fea and differential evolution,” *IEEE Transactions on Industry Applications*, vol. 49, no. 5, pp. 2086–2096, 2013.
- [28] G. Stumberger, D. Dolinar, U. Palmer, and K. Hameyer, “Optimization of radial active magnetic bearings using the finite element technique and the differential evolution algorithm,” *IEEE Transactions on Magnetica*, vol. 36, no. 4, pp. 1009–1013, 2000.
- [29] J. R. Hendershot and T. J. E. Miller, *Design of brushless permanent-magnet machines*. Motor Design Books, 2010.